

Measurement of elliptic flow of light nuclei at  $\sqrt{s_{NN}} = 200, 62.4, 39, 27, 19.6, 11.5,$   
and 7.7 GeV at RHIC

L. Adamczyk<sup>1</sup>, J. K. Adkins<sup>20</sup>, G. Agakishiev<sup>18</sup>, M. M. Aggarwal<sup>31</sup>, Z. Ahammed<sup>49</sup>, I. Alekseev<sup>16</sup>, A. Aparin<sup>18</sup>,  
D. Arkhipkin<sup>3</sup>, E. C. Aschenauer<sup>3</sup>, A. Attri<sup>31</sup>, G. S. Averichev<sup>18</sup>, X. Bai<sup>7</sup>, V. Bairathi<sup>27</sup>, R. Bellwied<sup>45</sup>,  
A. Bhasin<sup>17</sup>, A. K. Bhati<sup>31</sup>, P. Bhattarai<sup>44</sup>, J. Bielcik<sup>10</sup>, J. Bielcikova<sup>11</sup>, L. C. Bland<sup>3</sup>, I. G. Bordyuzhin<sup>16</sup>,  
J. Bouchet<sup>19</sup>, J. D. Brandenburg<sup>37</sup>, A. V. Brandin<sup>26</sup>, I. Bunzarov<sup>18</sup>, J. Butterworth<sup>37</sup>, H. Caines<sup>53</sup>,  
M. Calderón de la Barca Sánchez<sup>5</sup>, J. M. Campbell<sup>29</sup>, D. Cebra<sup>5</sup>, I. Chakaberia<sup>3</sup>, P. Chaloupka<sup>10</sup>, Z. Chang<sup>43</sup>,  
A. Chatterjee<sup>49</sup>, S. Chattopadhyay<sup>49</sup>, J. H. Chen<sup>40</sup>, X. Chen<sup>22</sup>, J. Cheng<sup>46</sup>, M. Cherney<sup>9</sup>, W. Christie<sup>3</sup>, G. Contin<sup>23</sup>,  
H. J. Crawford<sup>4</sup>, S. Das<sup>13</sup>, L. C. De Silva<sup>9</sup>, R. R. Debbé<sup>3</sup>, T. G. Dedovich<sup>18</sup>, J. Deng<sup>39</sup>, A. A. Derevschikov<sup>33</sup>,  
B. di Ruzza<sup>3</sup>, L. Didenko<sup>3</sup>, C. Dilks<sup>32</sup>, X. Dong<sup>23</sup>, J. L. Drachenberg<sup>48</sup>, J. E. Draper<sup>5</sup>, C. M. Du<sup>22</sup>,  
L. E. Dunkelberger<sup>6</sup>, J. C. Dunlop<sup>3</sup>, L. G. Efimov<sup>18</sup>, J. Engelage<sup>4</sup>, G. Eppley<sup>37</sup>, R. Esha<sup>6</sup>, O. Evdokimov<sup>8</sup>,  
O. Eyster<sup>3</sup>, R. Fatemi<sup>20</sup>, S. Fazio<sup>3</sup>, P. Federic<sup>11</sup>, J. Fedorisin<sup>18</sup>, Z. Feng<sup>7</sup>, P. Filip<sup>18</sup>, Y. Fisyak<sup>3</sup>, C. E. Flores<sup>5</sup>,  
L. Fulek<sup>1</sup>, C. A. Gagliardi<sup>43</sup>, D. Garand<sup>34</sup>, F. Geurts<sup>37</sup>, A. Gibson<sup>48</sup>, M. Girard<sup>50</sup>, L. Greiner<sup>23</sup>, D. Grosnick<sup>48</sup>,  
D. S. Gunarathne<sup>42</sup>, Y. Guo<sup>38</sup>, S. Gupta<sup>17</sup>, A. Gupta<sup>17</sup>, W. Guryn<sup>3</sup>, A. I. Hamad<sup>19</sup>, A. Hamed<sup>43</sup>, R. Haque<sup>27</sup>,  
J. W. Harris<sup>53</sup>, L. He<sup>34</sup>, S. Heppelmann<sup>5</sup>, S. Heppelmann<sup>32</sup>, A. Hirsch<sup>34</sup>, G. W. Hoffmann<sup>44</sup>, S. Horvat<sup>53</sup>,  
T. Huang<sup>28</sup>, X. Huang<sup>46</sup>, B. Huang<sup>8</sup>, H. Z. Huang<sup>6</sup>, P. Huck<sup>7</sup>, T. J. Humanic<sup>29</sup>, G. Igo<sup>6</sup>, W. W. Jacobs<sup>15</sup>,  
H. Jang<sup>21</sup>, A. Jentsch<sup>44</sup>, J. Jia<sup>3</sup>, K. Jiang<sup>38</sup>, E. G. Judd<sup>4</sup>, S. Kabana<sup>19</sup>, D. Kalinkin<sup>15</sup>, K. Kang<sup>46</sup>, K. Kauder<sup>51</sup>,  
H. W. Ke<sup>3</sup>, D. Keane<sup>19</sup>, A. Kechechyan<sup>18</sup>, Z. H. Khan<sup>8</sup>, D. P. Kikoła<sup>50</sup>, I. Kisel<sup>12</sup>, A. Kisiel<sup>50</sup>, L. Kochenda<sup>26</sup>,  
D. D. Koetke<sup>48</sup>, L. K. Kosarzewski<sup>50</sup>, A. F. Kraishan<sup>42</sup>, P. Kravtsov<sup>26</sup>, K. Krueger<sup>2</sup>, L. Kumar<sup>31</sup>,  
M. A. C. Lamont<sup>3</sup>, J. M. Landgraf<sup>3</sup>, K. D. Landry<sup>6</sup>, J. Lauret<sup>3</sup>, A. Lebedev<sup>3</sup>, R. Lednicky<sup>18</sup>, J. H. Lee<sup>3</sup>,  
X. Li<sup>42</sup>, C. Li<sup>38</sup>, X. Li<sup>38</sup>, Y. Li<sup>46</sup>, W. Li<sup>40</sup>, T. Lin<sup>15</sup>, M. A. Lisa<sup>29</sup>, F. Liu<sup>7</sup>, T. Ljubicic<sup>3</sup>, W. J. Llope<sup>51</sup>,  
M. Lomnitz<sup>19</sup>, R. S. Longacre<sup>3</sup>, X. Luo<sup>7</sup>, R. Ma<sup>3</sup>, G. L. Ma<sup>40</sup>, Y. G. Ma<sup>40</sup>, L. Ma<sup>40</sup>, N. Magdy<sup>41</sup>, R. Majka<sup>53</sup>,  
A. Manion<sup>23</sup>, S. Margetis<sup>19</sup>, C. Markert<sup>44</sup>, H. S. Matis<sup>23</sup>, D. McDonald<sup>45</sup>, S. McKinzie<sup>23</sup>, K. Meehan<sup>5</sup>, J. C. Mei<sup>39</sup>,  
N. G. Minaev<sup>33</sup>, S. Mioduszewski<sup>43</sup>, D. Mishra<sup>27</sup>, B. Mohanty<sup>27</sup>, M. M. Mondal<sup>43</sup>, D. A. Morozov<sup>33</sup>,  
M. K. Mustafa<sup>23</sup>, B. K. Nandi<sup>14</sup>, Md. Nasim<sup>6</sup>, T. K. Nayak<sup>49</sup>, G. Nigmatkulov<sup>26</sup>, T. Niida<sup>51</sup>, L. V. Nogach<sup>33</sup>,  
S. Y. Noh<sup>21</sup>, J. Novak<sup>25</sup>, S. B. Nurushev<sup>33</sup>, G. Odyniec<sup>23</sup>, A. Ogawa<sup>3</sup>, K. Oh<sup>35</sup>, V. A. Okorokov<sup>26</sup>, D. Olivitt Jr.<sup>42</sup>,  
B. S. Page<sup>3</sup>, R. Pak<sup>3</sup>, Y. X. Pan<sup>6</sup>, Y. Pandit<sup>8</sup>, Y. Panebratsev<sup>18</sup>, B. Pawlik<sup>30</sup>, H. Pei<sup>7</sup>, C. Perkins<sup>4</sup>, P. Pile<sup>3</sup>,  
J. Pluta<sup>50</sup>, K. Poniatowska<sup>50</sup>, J. Porter<sup>23</sup>, M. Posik<sup>42</sup>, A. M. Poskanzer<sup>23</sup>, N. K. Pruthi<sup>31</sup>, J. Putschke<sup>51</sup>,  
H. Qiu<sup>23</sup>, A. Quintero<sup>19</sup>, S. Ramachandran<sup>20</sup>, R. Raniwala<sup>36</sup>, S. Raniwala<sup>36</sup>, R. L. Ray<sup>44</sup>, H. G. Ritter<sup>23</sup>,  
J. B. Roberts<sup>37</sup>, O. V. Rogachevskiy<sup>18</sup>, J. L. Romero<sup>5</sup>, L. Ruan<sup>3</sup>, J. Rusnak<sup>11</sup>, O. Rusnakova<sup>10</sup>, N. R. Sahoo<sup>43</sup>,  
P. K. Sahu<sup>13</sup>, I. Sakrejda<sup>23</sup>, S. Salur<sup>23</sup>, J. Sandweiss<sup>53</sup>, A. Sarkar<sup>14</sup>, J. Schambach<sup>44</sup>, R. P. Scharenberg<sup>34</sup>,  
A. M. Schmah<sup>23</sup>, W. B. Schmidke<sup>3</sup>, N. Schmitz<sup>24</sup>, J. Seger<sup>9</sup>, P. Seyboth<sup>24</sup>, N. Shah<sup>40</sup>, E. Shalahiev<sup>18</sup>,  
P. V. Shanmuganathan<sup>19</sup>, M. Shao<sup>38</sup>, M. K. Sharma<sup>17</sup>, B. Sharma<sup>31</sup>, W. Q. Shen<sup>40</sup>, Z. Shi<sup>23</sup>, S. S. Shi<sup>7</sup>,  
Q. Y. Shou<sup>40</sup>, E. P. Sichtermann<sup>23</sup>, R. Sikora<sup>1</sup>, M. Simko<sup>11</sup>, S. Singha<sup>19</sup>, M. J. Skoby<sup>15</sup>, N. Smirnov<sup>53</sup>, D. Smirnov<sup>3</sup>,  
W. Solyst<sup>15</sup>, L. Song<sup>45</sup>, P. Sorensen<sup>3</sup>, H. M. Spinka<sup>2</sup>, B. Srivastava<sup>34</sup>, T. D. S. Stanislaus<sup>48</sup>, M. Stepanov<sup>34</sup>,  
R. Stock<sup>12</sup>, M. Strikhanov<sup>26</sup>, B. Stringfellow<sup>34</sup>, M. Sumera<sup>11</sup>, B. Summa<sup>32</sup>, X. M. Sun<sup>7</sup>, Z. Sun<sup>22</sup>, Y. Sun<sup>38</sup>,  
B. Surov<sup>42</sup>, D. N. Svirida<sup>16</sup>, Z. Tang<sup>38</sup>, A. H. Tang<sup>3</sup>, T. Tarnowsky<sup>25</sup>, A. Tawfik<sup>52</sup>, J. Thäder<sup>23</sup>, J. H. Thomas<sup>23</sup>,  
A. R. Timmins<sup>45</sup>, D. Tlusty<sup>37</sup>, T. Todoroki<sup>3</sup>, M. Tokarev<sup>18</sup>, S. Trentalange<sup>6</sup>, R. E. Tribble<sup>43</sup>, P. Tribedy<sup>3</sup>,  
S. K. Tripathy<sup>13</sup>, O. D. Tsai<sup>6</sup>, T. Ullrich<sup>3</sup>, D. G. Underwood<sup>2</sup>, I. Upsal<sup>29</sup>, G. Van Buren<sup>3</sup>, G. van Nieuwenhuizen<sup>3</sup>,  
M. Vandenbroucke<sup>42</sup>, R. Varma<sup>14</sup>, A. N. Vasiliev<sup>33</sup>, R. Vertesi<sup>11</sup>, F. Videbæk<sup>3</sup>, S. Vokal<sup>18</sup>, S. A. Voloshin<sup>51</sup>,  
A. Vossen<sup>15</sup>, Y. Wang<sup>7</sup>, G. Wang<sup>6</sup>, J. S. Wang<sup>22</sup>, H. Wang<sup>3</sup>, Y. Wang<sup>46</sup>, F. Wang<sup>34</sup>, G. Webb<sup>3</sup>, J. C. Webb<sup>3</sup>,  
L. Wen<sup>6</sup>, G. D. Westfall<sup>25</sup>, H. Wieman<sup>23</sup>, S. W. Wissink<sup>15</sup>, R. Witt<sup>47</sup>, Y. Wu<sup>19</sup>, Z. G. Xiao<sup>46</sup>, W. Xie<sup>34</sup>,  
G. Xie<sup>38</sup>, K. Xin<sup>37</sup>, H. Xu<sup>22</sup>, Z. Xu<sup>3</sup>, J. Xu<sup>7</sup>, Y. F. Xu<sup>40</sup>, Q. H. Xu<sup>39</sup>, N. Xu<sup>23</sup>, Y. Yang<sup>7</sup>, S. Yang<sup>38</sup>, C. Yang<sup>38</sup>,  
Y. Yang<sup>22</sup>, Y. Yang<sup>28</sup>, Q. Yang<sup>38</sup>, Z. Ye<sup>8</sup>, Z. Ye<sup>8</sup>, P. Yepes<sup>37</sup>, L. Yi<sup>53</sup>, K. Yip<sup>3</sup>, I. -K. Yoo<sup>35</sup>, N. Yu<sup>7</sup>,  
H. Zbroszczyk<sup>50</sup>, W. Zha<sup>38</sup>, J. Zhang<sup>39</sup>, Y. Zhang<sup>38</sup>, X. P. Zhang<sup>46</sup>, Z. Zhang<sup>40</sup>, J. B. Zhang<sup>7</sup>, S. Zhang<sup>38</sup>,  
S. Zhang<sup>40</sup>, J. Zhang<sup>22</sup>, J. Zhao<sup>34</sup>, C. Zhong<sup>40</sup>, L. Zhou<sup>38</sup>, X. Zhu<sup>46</sup>, Y. Zoulkarneeva<sup>18</sup>, M. Zyzak<sup>12</sup>

<sup>1</sup>AGH University of Science and Technology, FPACS, Cracow 30-059, Poland

<sup>2</sup>Argonne National Laboratory, Argonne, Illinois 60439

<sup>3</sup>Brookhaven National Laboratory, Upton, New York 11973

<sup>4</sup>University of California, Berkeley, California 94720

<sup>5</sup>University of California, Davis, California 95616

<sup>6</sup>University of California, Los Angeles, California 90095

<sup>7</sup>Central China Normal University, Wuhan, Hubei 430079

- <sup>8</sup>University of Illinois at Chicago, Chicago, Illinois 60607  
<sup>9</sup>Creighton University, Omaha, Nebraska 68178  
<sup>10</sup>Czech Technical University in Prague, FNSPE, Prague, 115 19, Czech Republic  
<sup>11</sup>Nuclear Physics Institute AS CR, 250 68 Prague, Czech Republic  
<sup>12</sup>Frankfurt Institute for Advanced Studies FIAS, Frankfurt 60438, Germany  
<sup>13</sup>Institute of Physics, Bhubaneswar 751005, India  
<sup>14</sup>Indian Institute of Technology, Mumbai 400076, India  
<sup>15</sup>Indiana University, Bloomington, Indiana 47408  
<sup>16</sup>Alikhanov Institute for Theoretical and Experimental Physics, Moscow 117218, Russia  
<sup>17</sup>University of Jammu, Jammu 180001, India  
<sup>18</sup>Joint Institute for Nuclear Research, Dubna, 141 980, Russia  
<sup>19</sup>Kent State University, Kent, Ohio 44242  
<sup>20</sup>University of Kentucky, Lexington, Kentucky, 40506-0055  
<sup>21</sup>Korea Institute of Science and Technology Information, Daejeon 305-701, Korea  
<sup>22</sup>Institute of Modern Physics, Chinese Academy of Sciences, Lanzhou, Gansu 730000  
<sup>23</sup>Lawrence Berkeley National Laboratory, Berkeley, California 94720  
<sup>24</sup>Max-Planck-Institut für Physik, Munich 80805, Germany  
<sup>25</sup>Michigan State University, East Lansing, Michigan 48824  
<sup>26</sup>National Research Nuclear University MEPhI, Moscow 115409, Russia  
<sup>27</sup>National Institute of Science Education and Research, Bhubaneswar 751005, India  
<sup>28</sup>National Cheng Kung University, Tainan 70101  
<sup>29</sup>Ohio State University, Columbus, Ohio 43210  
<sup>30</sup>Institute of Nuclear Physics PAN, Cracow 31-342, Poland  
<sup>31</sup>Panjab University, Chandigarh 160014, India  
<sup>32</sup>Pennsylvania State University, University Park, Pennsylvania 16802  
<sup>33</sup>Institute of High Energy Physics, Protvino 142281, Russia  
<sup>34</sup>Purdue University, West Lafayette, Indiana 47907  
<sup>35</sup>Pusan National University, Pusan 46241, Korea  
<sup>36</sup>University of Rajasthan, Jaipur 302004, India  
<sup>37</sup>Rice University, Houston, Texas 77251  
<sup>38</sup>University of Science and Technology of China, Hefei, Anhui 230026  
<sup>39</sup>Shandong University, Jinan, Shandong 250100  
<sup>40</sup>Shanghai Institute of Applied Physics, Chinese Academy of Sciences, Shanghai 201800  
<sup>41</sup>State University Of New York, Stony Brook, NY 11794  
<sup>42</sup>Temple University, Philadelphia, Pennsylvania 19122  
<sup>43</sup>Texas A&M University, College Station, Texas 77843  
<sup>44</sup>University of Texas, Austin, Texas 78712  
<sup>45</sup>University of Houston, Houston, Texas 77204  
<sup>46</sup>Tsinghua University, Beijing 100084  
<sup>47</sup>United States Naval Academy, Annapolis, Maryland, 21402  
<sup>48</sup>Valparaiso University, Valparaiso, Indiana 46383  
<sup>49</sup>Variable Energy Cyclotron Centre, Kolkata 700064, India  
<sup>50</sup>Warsaw University of Technology, Warsaw 00-661, Poland  
<sup>51</sup>Wayne State University, Detroit, Michigan 48201  
<sup>52</sup>World Laboratory for Cosmology and Particle Physics (WLCAPP), Cairo 11571, Egypt and  
<sup>53</sup>Yale University, New Haven, Connecticut 06520

(STAR Collaboration)

We present measurements of 2<sup>nd</sup> order azimuthal anisotropy ( $v_2$ ) at mid-rapidity ( $|y| < 1.0$ ) for light nuclei d, t,  $^3\text{He}$  (for  $\sqrt{s_{NN}} = 200, 62.4, 39, 27, 19.6, 11.5,$  and  $7.7$  GeV) and anti-nuclei  $\bar{d}$  ( $\sqrt{s_{NN}} = 200, 62.4, 39, 27,$  and  $19.6$  GeV) and  $^3\bar{\text{He}}$  ( $\sqrt{s_{NN}} = 200$  GeV) in the STAR (Solenoidal Tracker at RHIC) experiment. The  $v_2$  for these light nuclei produced in heavy-ion collisions is compared with those for p and  $\bar{p}$ . We observe mass ordering in nuclei  $v_2(p_T)$  at low transverse momenta ( $p_T < 2.0$  GeV/c). We also find a centrality dependence of  $v_2$  for d and  $\bar{d}$ . The magnitude of  $v_2$  for t and  $^3\text{He}$  agree within statistical errors. Light-nuclei  $v_2$  are compared with predictions from a blast wave model. Atomic mass number ( $A$ ) scaling of light-nuclei  $v_2(p_T)$  seems to hold for  $p_T/A < 1.5$  GeV/c. Results on light-nuclei  $v_2$  from a transport-plus-coalescence model are consistent with the experimental measurements.

## I. INTRODUCTION

One of the main goals of high energy heavy-ion collision experiments is to study phase structures in the

QCD phase diagram [1, 2]. With this purpose the Relativistic Heavy Ion Collider (RHIC) has finished the first phase of the Beam Energy Scan (BES) program [3–9].

It has been found that the identified hadron  $v_2$  shows number-of-constituent-quark (NCQ) scaling at high  $p_T$  at the higher beam energies. This scaling behavior is an expected signature of partonic collectivity via quark coalescence in the strongly interacting medium of quarks and gluons formed in heavy-ion collisions [10–14]. Such a scaling behavior also suggests partonic coalescence to be a mechanism for hadron formation [10, 11, 15]. In a relativistic heavy-ion collision, light (anti-)nuclei can be formed by coalescence of produced (anti-)nucleons or from transported nucleons [16–18]. The binding energies of light nuclei are very small ( $\sim$  few MeV), making it likely that surviving light nuclei are formed at a later stage of the evolution. This phenomenon is called final-state coalescence [16, 19]. The coalescence probability of two nucleons is related to the local nucleon density [16, 17, 20]. Since the coalescence mechanism works best at the low density limit, low relative production of nucleons in heavy-ion collisions offers an ideal situation to study light-nuclei production via coalescence. Measurements of azimuthal anisotropy of light nuclei offers a tool to understand the light-nuclei production mechanism and freeze-out properties at a later stage of the evolution. Unlike the case of quark coalescence, in a nucleon coalescence, the momentum space distributions of both the constituents and the products are measurable in heavy-ion collision experiments.

Prior measurements of elliptic flow ( $v_2$ ) of light nuclei have been carried out at the top RHIC energy ( $\sqrt{s_{NN}} = 200$  GeV) by the PHENIX [21] and the STAR [22, 23] experiments. The PHENIX Collaboration has measured the  $v_2$  of deuterons (d) and anti-deuterons ( $\bar{d}$ ) at intermediate transverse momenta ( $1.1 < p_T < 4.5$  GeV/c). How the  $v_2$  of these light nuclei scale with those of (anti-)protons also has been reported [21]. The STAR collaboration has measured the  $v_2$  of d,  $\bar{d}$ ,  ${}^3\text{He}$ , and  ${}^3\bar{\text{He}}$  in Au+Au collisions at  $\sqrt{s_{NN}} = 200$  GeV in the years 2004 [22] and 2007 [23]. Negative  $v_2$  for  $\bar{d}$  at low  $p_T$  has also been reported [22].

In this work we expand upon previous studies with a detailed investigation on the energy and centrality dependence of  $v_2$  of light nuclei with more event statistics. During the BES program, the STAR experiment has taken data over a wide range of collision energies from  $\sqrt{s_{NN}} = 7.7$  GeV to 200 GeV. In this paper we present the measurement of  $v_2$  at mid-rapidity ( $|y| < 1.0$ ) for light nuclei d, t,  ${}^3\text{He}$  ( $\sqrt{s_{NN}} = 200, 62.4, 39, 27, 19.6, 11.5$ , and 7.7 GeV), and anti-nuclei  $\bar{d}$  ( $\sqrt{s_{NN}} = 200, 62.4, 39, 27$ , and 19.6 GeV) and  ${}^3\bar{\text{He}}$  ( $\sqrt{s_{NN}} = 200$  GeV)

The paper is organized as follows. Sec. II briefly describes the experimental setup, the detectors and the particle (and light-nuclei) identification (PID) techniques. The centrality definition, event selection, event plane reconstruction and the event plane resolution correction are also discussed, along with the extraction procedure of light-nuclei  $v_2$ . Presented in Sec. III are the  $v_2$  results for minimum bias collisions, the centrality dependence, and a physical interpretation of the results. A compari-

son between light-nuclei  $v_2$  measured in this experiment and those calculated from blast wave and transport-plus-coalescence model is also shown. Sec. IV summarizes the physics observations and discusses the main conclusions from the results.

## II. EXPERIMENTAL SETUP

STAR is a multipurpose experiment at the RHIC facility at Brookhaven National Laboratory. It consists of a longitudinally-oriented (beam direction) solenoidal magnet and a collection of detectors for triggering, PID, and event categorization [24]. The main detectors used for this analysis are the Time Projection Chamber (TPC) [25] and the Time of Flight (TOF) detector [26]. The following subsections briefly describe their operations and PID techniques.

### A. TPC Measurements

The TPC is the primary tracking device in the STAR experiment which uses ionisation in a large gas volume to detect trajectories of charged particles. Curvature in the solenoidal field enables determination of the charge sign and rigidity (momentum/charge). The TPC has full azimuthal coverage and a uniform pseudorapidity range of  $|\eta| < 1.0$  [25]. The TPC can record up to 45 hit positions and specific ionisation energy loss (dE/dx) samples along tracks. Truncated means of the dE/dx samples are used for PID by comparing to theoretical expectations, using improved Bethe-Bloch functions [27], at the measured rigidities to characterize the probability for being any particular species. PID consequently allows deduction of the particles' charges and momenta. A representative plot of measured track dE/dx versus rigidity is shown in Fig. 1(a) for minimum bias (defined later) Au+Au collisions at  $\sqrt{s_{NN}} = 19.6$  GeV. The theoretical curves are shown as solid lines. Primary collision vertices are found through fits involving candidate daughter tracks, and a typical central collision at the top RHIC energy (with perhaps  $\sim 1000$  reconstructed tracks) may achieve a vertex position resolution of  $\sim 350$   $\mu\text{m}$ . These daughter tracks are then refitted using their vertex as a constraint to create a collection of primary tracks.

### B. TOF Measurements

The TOF detector [26] in STAR uses Multigap Resistive Plate Chambers (MRPCs) and was fully installed in the year 2010. It covers  $2\pi$  in azimuth within the pseudorapidity interval  $|\eta| < 0.94$ . The TOF detector and the Vertex Position Detector (VPD) [28] measure the time interval,  $t$ , over which a particle travels from the primary collision vertex to a read-out cell of the TOF detector. This time interval information is combined with

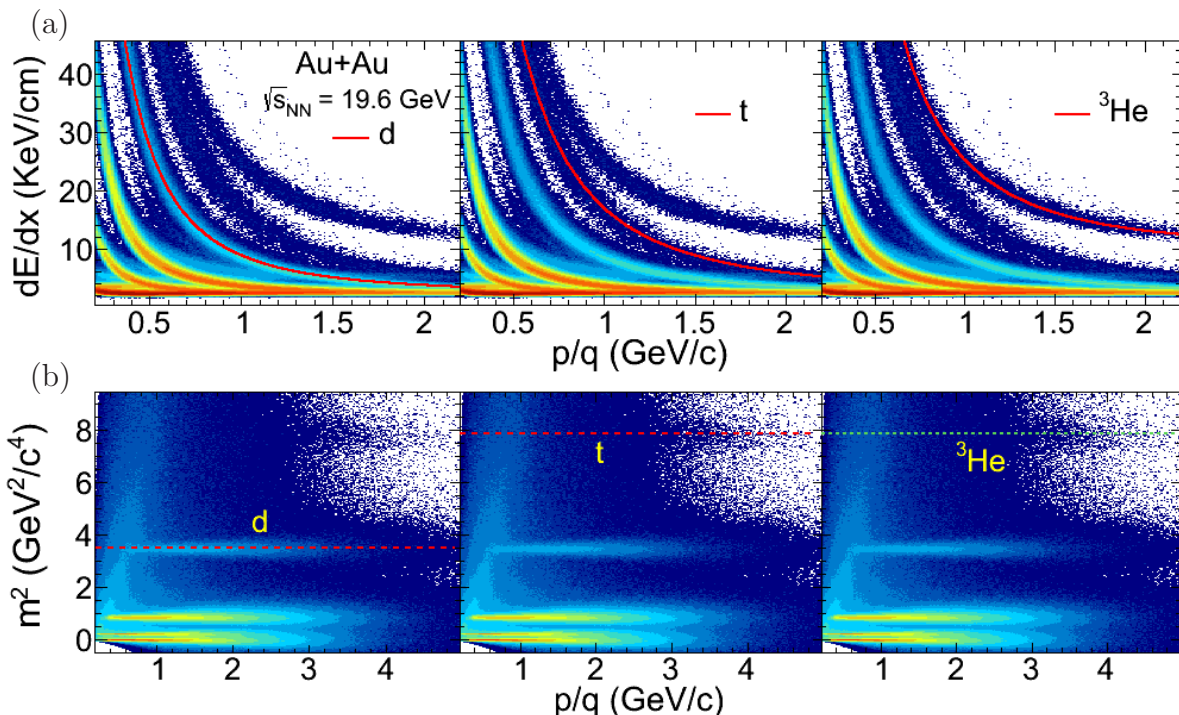


FIG. 1. (color online) (a) Specific energy loss ( $dE/dx$ ) as a function of rigidity (momentum/charge). Theoretical  $dE/dx$  expectations, using the model in Ref. [27] of  $d$ ,  $t$ ,  ${}^3\text{He}$  are shown by solid curves. (b) Mass squared ( $m^2$ ) as a function of momentum for mid-rapidity charged particles. The dotted lines correspond to  $m^2$  of different nuclei. Both results are from minimum bias Au+Au collisions at  $\sqrt{s_{NN}} = 19.6$  GeV.

the total path length,  $S$ , measured by the TPC to provide the inverse velocity,  $1/\beta$ , via  $1/\beta = ct/S$ , where  $c$  is the speed of light. The track mass-squared is then given by  $m^2 = p^2(1/\beta^2 - 1)$ . For collision energies below  $\sqrt{s_{NN}} = 39$  GeV the VPD efficiency is too low to use in every event. Instead, for these data sets a start time for each collision is inferred by working backwards from the TOF-measured stop times of a very limited selection of particles which are very cleanly identified in the TPC. The total time interval resolution obtained of 90-110 ps results in PID capabilities that are complementary to those from the TPC  $dE/dx$  at low momenta and also extend to momenta of several GeV. A representative plot of  $m^2$  as a function of the particle momentum is shown in Fig. 1(b) for minimum bias Au+Au collisions at  $\sqrt{s_{NN}} = 19.6$  GeV. As the mass of a particle is a constant quantity, we expect horizontal bands for individual (anti-)nuclei as shown by the dotted lines in Fig. 1(b). We have selected individual nuclei using the  $m^2$  which lie within  $3\sigma$  from the constant mean (dotted line).

### C. Trigger and event selection

The minimum bias events for all of the collision energies are based on a coincidence of the signals from the Zero-Degree Calorimeters (ZDC) [29], VPD, and/or Beam-Beam Counters (BBC) [30]. Due to larger beam

emittance at lower collision energies, Au+Au-triggered events are contaminated with Au+beam-pipe events. The radius of the beam-pipe going through the center of the TPC is 3.95 cm. Therefore, such Au+beam-pipe events are removed by requiring the primary vertex position to be within a transverse radius of less than 2 cm in the XY-plane [4]. The  $z$ -position of the primary vertices (vertex- $z$ ) is limited to the values listed in Table I [4] to ensure good quality events.

TABLE I. The vertex- $z$  acceptance and total number of minimum-bias (MB) events for each energy ( $\sqrt{s_{NN}}$ ).

$\sqrt{s_{NN}}$ (GeV)	vertex- $z$ (cm)	MB events ( $\times 10^6$ )
200	vertex- $z$   < 30	241
62.4	vertex- $z$   < 40	62
39	vertex- $z$   < 40	119
27	vertex- $z$   < 70	60
19.6	vertex- $z$   < 70	33
11.5	vertex- $z$   < 50	11
7.7	vertex- $z$   < 70	4

Furthermore, an extensive quality assurance of the events was performed based on the mean transverse momenta, the mean vertex position, the mean interaction rate, and the mean multiplicity in the detector. Run periods were removed if one of those quantities was more

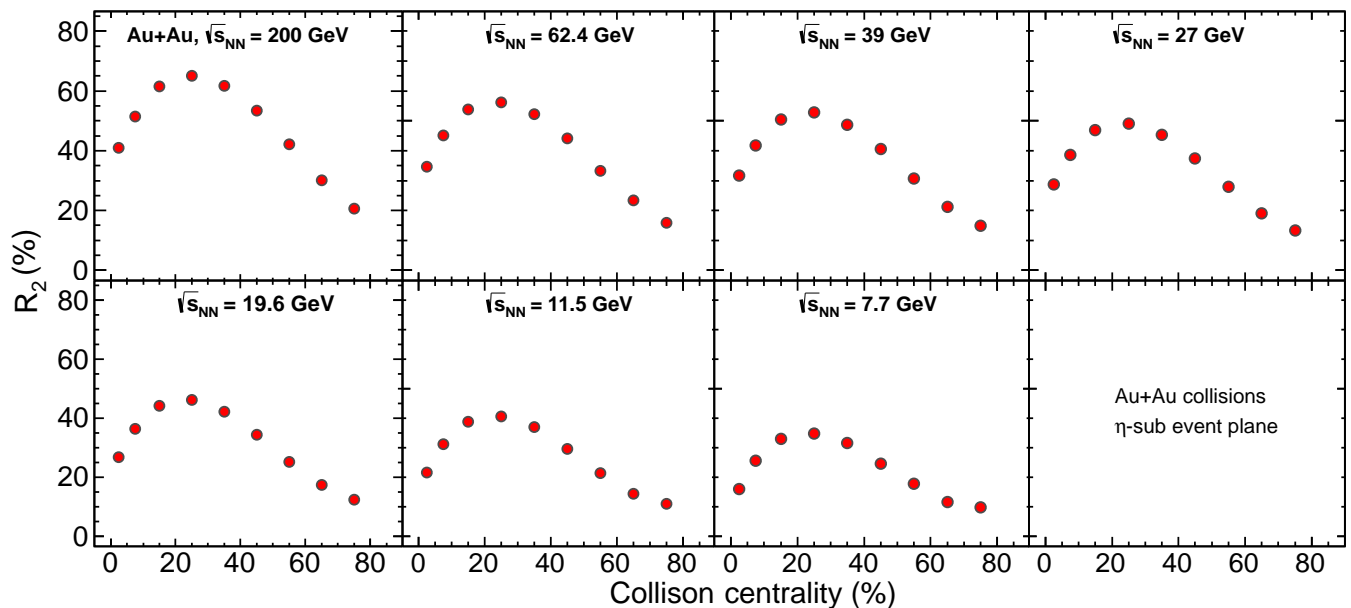


FIG. 2. Resolution correction factor ( $R_2$ ) of sub-event planes as a function of centrality for Au+Au collisions at  $\sqrt{s_{NN}} = 200, 62.4, 39, 27, 19.6, 11.5,$  and  $7.7$  GeV.

than  $3\sigma$  away from the global mean value. The total number of minimum bias events used in this analysis after these quality assurance cuts for each collision energy are shown in Table I.

#### D. Centrality definition

The centrality of each event is defined based on the uncorrected charged particle multiplicity ( $dN_{events}/dN_{charge}^{raw}$ ) distribution, where  $N_{events}$  is the number of events and  $N_{charge}^{raw}$  is the number of charged particles measured within  $|\eta| < 0.5$  [4]. Thus, for example, 0%-5% central events correspond to the events in the top 5% of the multiplicity distribution. The charged particle multiplicity distributions for all energies can be described by a two-component model [31]. The two-component model is a Glauber Monte-Carlo simulation in which the multiplicity per unit pseudo-rapidity ( $dN_{charge}/d\eta$ ) depends on the two components, namely, number of participant nucleons ( $N_{part}$ ) and number of binary collisions ( $N_{coll}$ ):

$$\frac{dN_{charge}}{d\eta} = n_{pp}[(1-x)\frac{N_{part}}{2} + xN_{coll}]. \quad (1)$$

The fitting parameter  $n_{pp}$  is the  $dN_{charge}/d\eta$  in minimum-bias p+p collisions and  $x$  is the fraction of produced charged particles from the hard component. The centrality class is defined by calculating the fraction of the total cross-section obtained from the simulated multiplicity. Due to trigger inefficiencies, many of the most peripheral events were not recorded. This results in a

significant difference between the measured distribution of charged particle multiplicities and the Glauber Monte Carlo (MC) simulation for peripheral collisions. When determining  $v_2$  in a bin of multiplicity wide enough to see variation in the trigger inefficiency across the bin (e.g. for a minimum bias measurement), it is necessary to compensate for this variation by weighting particle yields in each event by the inverse of the trigger efficiency at that event's multiplicity [4]. The correction is about 5% for the peripheral (70%-80%) events, and becomes negligible for central events. However, the corrections are severe for 80%-100% central events. Therefore, 80%-100% central events are not included in the current analysis, and minimum bias is defined for all data presented here as 0%-80%. In addition to the trigger inefficiency, two additional corrections are also applied to account for the vertex- $z$  dependent inefficiencies. These corrections account for the acceptance and detector inefficiencies and the time-dependent changes in  $dN_{events}/dN_{charge}^{raw}$ .

#### E. Event plane and resolution correction

The azimuthal distribution of produced particles with respect to reaction plane angle ( $\Psi_r$ ) can be expressed in terms of a Fourier series,

$$\frac{dN}{d(\phi - \Psi_r)} \propto 1 + 2v_1 \cos(\phi - \Psi_r) + 2v_2 \cos(2(\phi - \Psi_r)) + \dots \quad (2)$$

where  $\phi$  is the azimuthal angle of the produced particle.  $\Psi_r$  is defined as the angle between  $x$ -axis in the laboratory frame and axis of the impact parameter. Because we

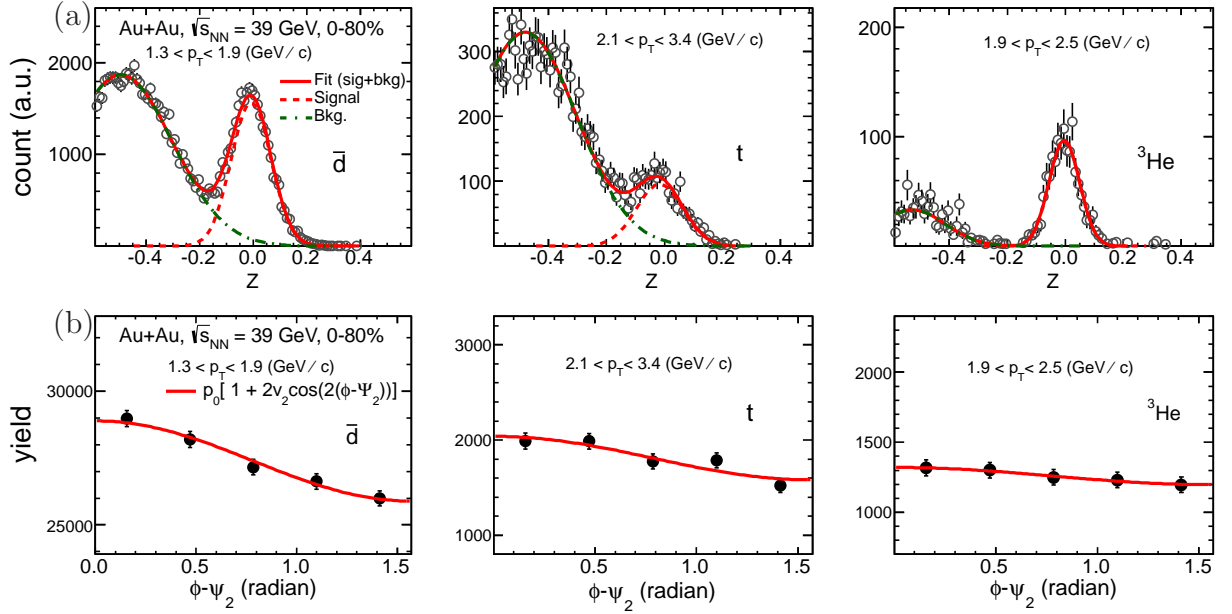


FIG. 3. (color online) (a)  $Z$  distributions for mid-rapidity  $\bar{d}$ ,  $t$ ,  ${}^3\text{He}$ . The different  $p_T$  ranges are for acceptance-representative purpose. The  $Z$  distribution for each species is fitted with a two-Gaussian function. One Gaussian is used to describe the  $Z$  distribution for the species of interest (dashed line), and another Gaussian is used to describe the background (dot-dashed line). (b)  $(\phi - \Psi_2)$  distributions for mid-rapidity  $\bar{d}$ ,  $t$ , and  ${}^3\text{He}$ . Solid lines are fitted 2<sup>nd</sup> order Fourier functions. All plots use minimum bias Au+Au collisions at  $\sqrt{s_{NN}} = 39$  GeV.

cannot directly measure  $\Psi_r$ , we must use a proxy. The second order azimuthal anisotropy or elliptic flow ( $v_2$ ) is measured with respect to the 2<sup>nd</sup> order event plane angle ( $\Psi_2$ ) instead.  $\Psi_2$  is calculated using the azimuthal distribution of all reconstructed primary tracks ( $N$ ) [32]:

$$\Psi_2 = \frac{1}{2} \tan^{-1} \left( \frac{Q_{2,y}}{Q_{2,x}} \right). \quad (3)$$

$Q_{2,x}$  and  $Q_{2,y}$  are defined as

$$Q_2 \cos(2\Psi_2) = Q_{2,x} = \sum_{i=1}^N w_i \cos(2\phi_i), \quad (4a)$$

$$Q_2 \sin(2\Psi_2) = Q_{2,y} = \sum_{i=1}^N w_i \sin(2\phi_i), \quad (4b)$$

where  $w_i$  are the weights which optimise the event plane resolution [32]. In this analysis, the weights scale with track- $p_T$ , then saturate above 2.0 GeV/c. To reduce biases due to short range correlation, we utilize the sub-event plane method [32]. In this analysis, the two sub-events were defined in  $\eta$  windows of  $\eta^-$  ( $-1.0 < \eta < -0.05$ ) and  $\eta^+$  ( $0.05 < \eta < 1.0$ ). Event plane angles are calculated within each  $\eta$  window,  $\Psi_{2\eta^-}$  and  $\Psi_{2\eta^+}$  respectively, and  $v_2$  is calculated in each sub-event using the opposite sub-event's event plane angle. The  $\eta$  gap ( $\Delta\eta = 0.1$ ) between the sub-events reduces the short range non-flow contributions and avoids the self-correlation. However, long range correlations may persist [33].

Due to the acceptance inefficiency of the detectors, the reconstructed event plane distributions are not uniform. Therefore, we apply event-by-event recenter [34] and shift [35] corrections. Finite multiplicities also restrict the degree to which the found event plane angles coincide with the true reaction plane angle. Hence, a resolution correction is applied to the observed elliptic flow ( $v_2^{obs}$ ):  $v_2 = v_2^{obs}/R_2$ . We determine the resolution correction factor ( $R_2$ ) in the  $\eta$  sub-event plane method as follows [32]:

$$R_2 = \sqrt{\langle \cos[2(\Psi_{2\eta^+} - \Psi_{2\eta^-})] \rangle}. \quad (5)$$

The resolution as a function of centrality for  $\eta$  sub-event planes is shown in Fig. 2 for Au+Au collisions.  $R_2$  grows with increasing multiplicity (which is small for peripheral collisions) and with increasing  $v_2$  (which is small for the most central collisions), so its value peaks in mid-central (20%-30%) collisions where neither is small.

## F. Extraction of yield and $v_2$ of nuclei

To identify light nuclei, we define a variable  $Z$  such that

$$Z = \ln[(dE/dx)_{\text{expt}}/(dE/dx)_{\text{theory}}], \quad (6)$$

where  $(dE/dx)_{\text{expt}}$  is the energy loss of the light nuclei measured by the TPC detector in the experiment and

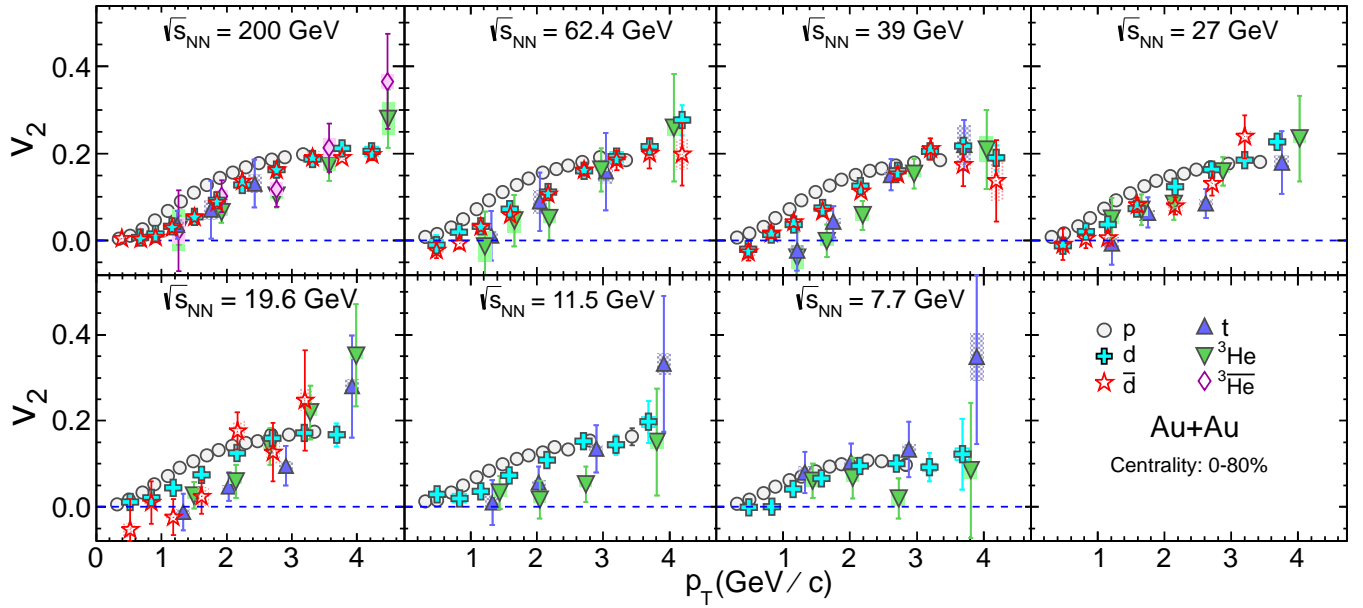


FIG. 4. (color online) Mid-rapidity  $v_2(p_T)$  for  $d$ ,  $\bar{d}$ ,  $t$ ,  ${}^3\text{He}$ , and  $\bar{{}^3\text{He}}$  from minimum bias Au+Au collisions at  $\sqrt{s_{NN}} = 200, 62.4, 39, 27, 19.6, 11.5,$  and  $7.7$  GeV. For comparison, proton  $v_2(p_T)$  are also shown as open circles [4, 9]. Lines and boxes at each marker represent statistical and systematic errors respectively.

$(dE/dx)_{\text{theory}}$  is the theoretical energy loss as obtained from the modified Bethe-Bloch formula [27]. After cutting on  $m^2$  from TOF (see Fig. 1(b)) to reduce backgrounds under the signals, the yields are extracted from the  $Z$  distributions in various  $p_T$  and  $(\phi - \Psi_2)$  bins for each species of interest with a two-Gaussian function (one for the signal, the other for the background). Figure 3(a) shows sample  $Z$  distributions for  $\bar{d}$ ,  $t$  and  ${}^3\text{He}$ , respectively, within  $0 < (\phi - \Psi_2) < \pi/10$  for  $1.3 < p_T < 1.9$  GeV/ $c$ ,  $2.1 < p_T < 3.4$  GeV/ $c$ , and  $1.9 < p_T < 2.5$  GeV/ $c$  for minimum bias Au+Au data at  $\sqrt{s_{NN}} = 39$  GeV. The azimuthal angle variation of this yield is then fitted with a  $2^{\text{nd}}$  order Fourier function to get the elliptic flow coefficient ( $v_2^{\text{obs}}$ ). Figure 3(b) shows the  $(\phi - \Psi_2)$  distributions for  $\bar{d}$ ,  $t$  and  ${}^3\text{He}$  for the same  $p_T$  ranges as shown for  $Z$  distributions in Fig. 3(a). As the  $(\phi - \Psi_2)$  distribution is expected to be symmetric about 0 and  $\pi/2$ , the data points have been folded onto  $0-\pi/2$  to reduce the statistical errors.

The fitted  $2^{\text{nd}}$  order Fourier functions are shown in Fig. 3(b). Event plane resolution correction factors are determined in each centrality bin. For  $v_2$  integrated over multiple centrality bins, species-yield-weighted mean of the individual centrality bins' resolutions are used:  $v_2 = v_2^{\text{obs}} \langle \frac{1}{R_2} \rangle$  [36].

### G. Calculation of systematic uncertainty and removal of beam-pipe contaminations

We have reduced light-nuclei contaminants from interactions with the beam pipe by cutting tightly on the pro-

jected distance of closest approach (DCA) to the primary vertex. Remaining contaminants from such interactions are removed statistically by fitting the DCA distribution of nuclei with that of anti-nuclei (which are expected to have no such background) in each  $(\phi - \Psi_2)$  bin. Systematic uncertainties are determined by varying cuts used in particle identification and background rejection, and by varying fitting methods and ranges when measuring yields. The absolute magnitude of uncertainties range from 2%-5% for intermediate  $p_T$  ( $1.0 < p_T < 3.0$  GeV/ $c$ ) and from 5%-8% for low and high  $p_T$ .

## III. RESULTS AND DISCUSSION

### A. General properties of $v_2(p_T)$

Figure 4 shows the energy dependence of the  $v_2$  of the light (anti-)nuclei  $d$ ,  $\bar{d}$ ,  $t$ ,  ${}^3\text{He}$ , and  $\bar{{}^3\text{He}}$  as a function of  $p_T$  for minimum bias Au+Au collisions. Insufficient statistics preclude measuring differential anti-nuclei  $v_2$  at several collision energies. The  $v_2(p_T)$  of all light-nuclei species and anti-nuclei species ( $\bar{d}$  at  $\sqrt{s_{NN}} = 19.6 - 200$  GeV and  $\bar{{}^3\text{He}}$  at  $\sqrt{s_{NN}} = 200$  GeV) show monotonically increasing trend with increasing  $p_T$  (Fig. 4). Mass ordering of  $v_2(p_T)$  for  $p_T < 2.0$  GeV/ $c$  is clear in both Figs. 4 and 5, where the  $v_2(p_T)$  of  $\pi^+$ ,  $K_s^0$ , and  $p$  from Ref. [4, 9] are also included (heavier species have a lower  $v_2$  in this  $p_T$  range). Such ordering occurs naturally in a hydrodynamic + coalescence model of heavy-ion collisions [37]. The negative  $v_2$  observed for some (anti-)nuclei could be

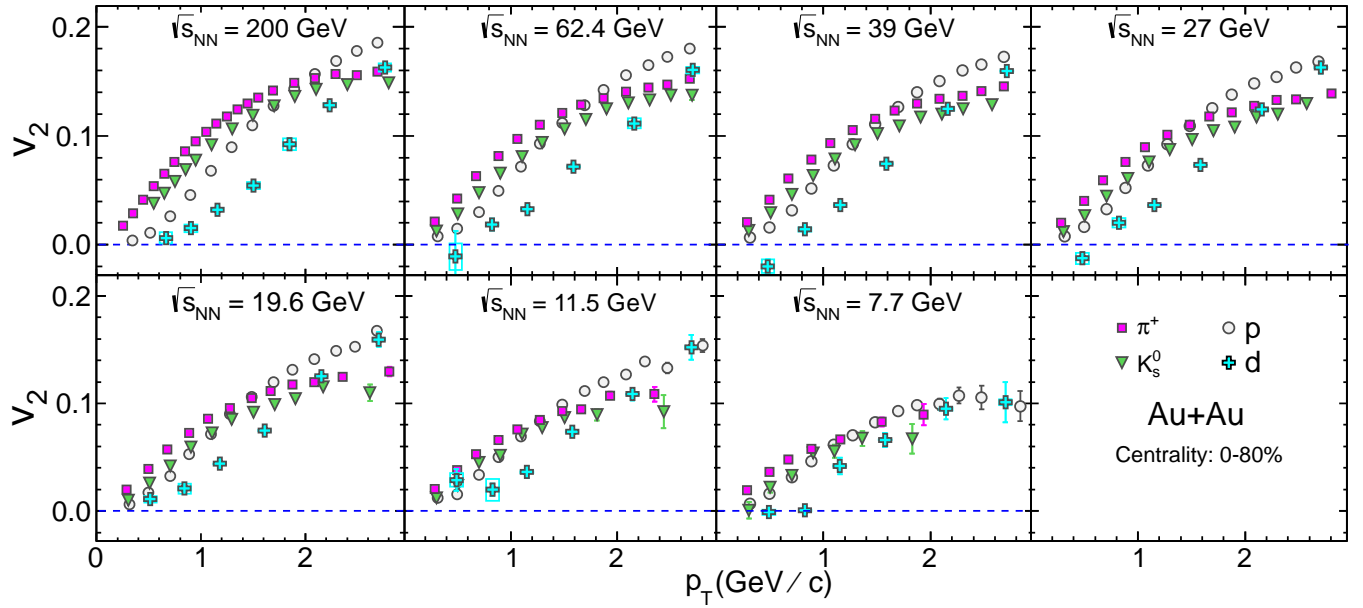


FIG. 5. (color online) Mid-rapidity  $v_2(p_T)$  for  $\pi^+$  (squares),  $K_s^0$  (triangles), p (open circles), and d (crosses) for minimum bias Au+Au collisions at  $\sqrt{s_{NN}} = 200, 62.4, 39, 27, 19.6, 11.5,$  and  $7.7$  GeV.

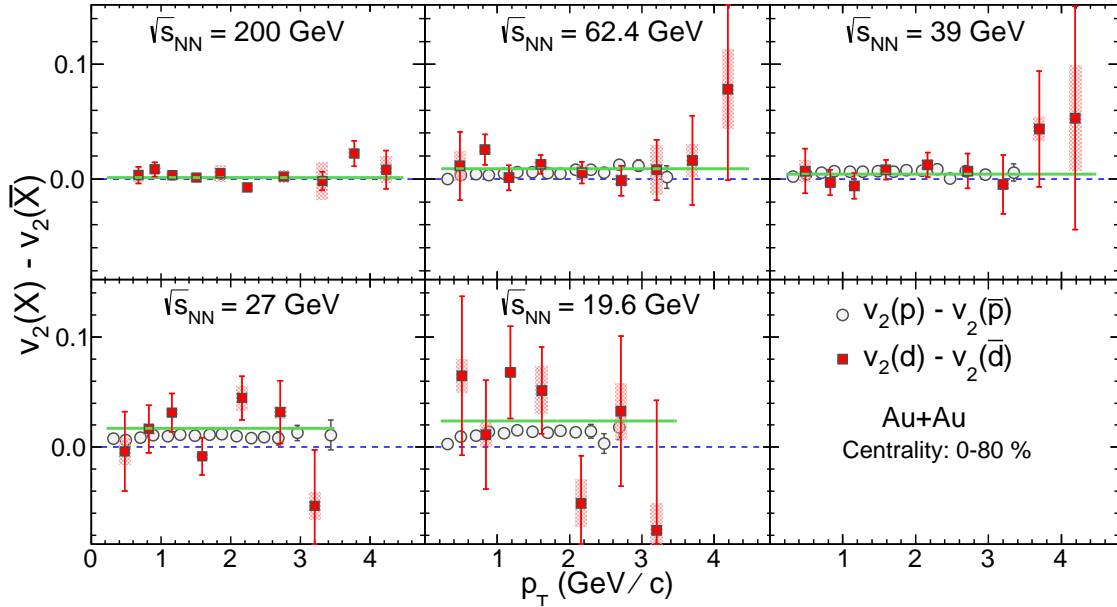


FIG. 6. (color online) The difference in  $v_2$  of d and  $\bar{d}$  as a function of  $p_T$  for minimum bias Au+Au collisions at  $\sqrt{s_{NN}} = 200, 62.4, 39, 27,$  and  $19.6$  GeV, along with differences between p and  $\bar{p}$  [4]. Solid lines correspond to constants fit to the data (see text for details).

the result of radial flow.

Figure 6 presents the difference of  $v_2(p_T)$  between d and  $\bar{d}$  ( $\Delta v_2$ ), along with the difference between p and  $\bar{p}$  for comparison [4, 9]. Statistical uncertainties are too large to draw conclusions about any collision energy dependence, but the  $\Delta v_2$  data are qualitatively consistent with the (anti-)protons and the results of fitting a constant at each energy (solid lines in Fig. 6) are consistently

positive:  $0.0012 \pm 0.0014$ ,  $0.009 \pm 0.005$ ,  $0.0044 \pm 0.0046$ ,  $0.017 \pm 0.009$ ,  $0.024 \pm 0.019$  for  $\sqrt{s_{NN}} = 200, 62.4, 39, 27,$  and  $19.6$  GeV respectively.

Figure 7 shows  $v_2(p_T)$  of d and  $\bar{d}$  in 0%-30% and 30%-80% central events for where they could be measured in Au+Au collisions at  $\sqrt{s_{NN}} = 62.4$  to  $7.7$  GeV. For 200 GeV  $v_2$  are measured in three centralities: 0%-10%, 10%-40%, and 40%-80%. The observed centrality depen-



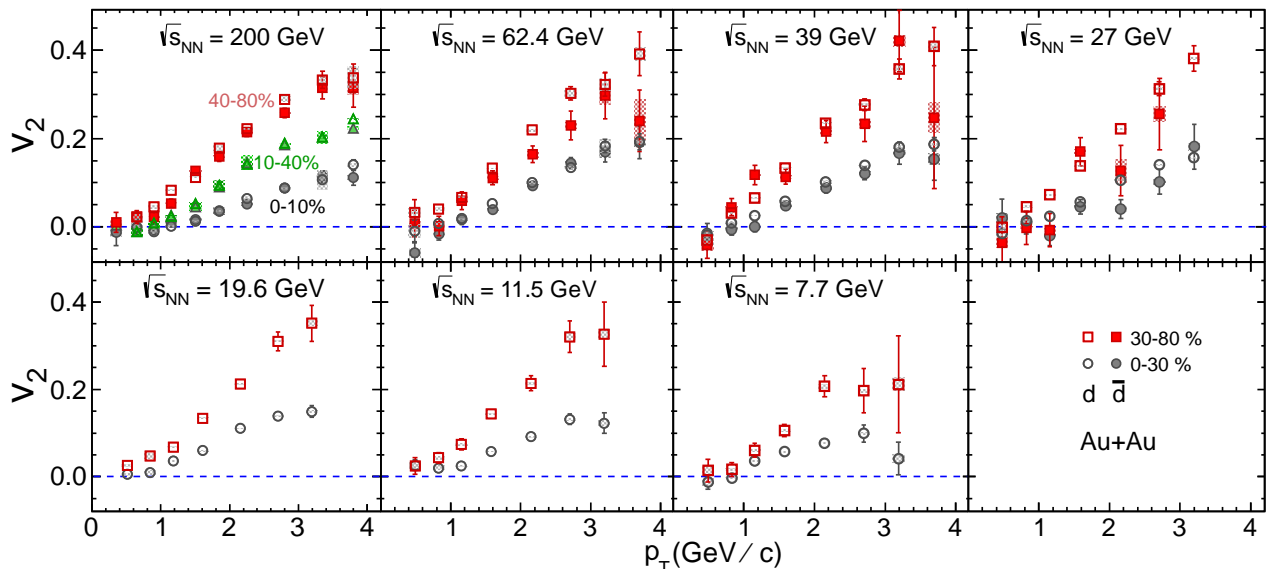


FIG. 7. (color online) Centrality dependence of mid-rapidity  $v_2(p_T)$  of d (open markers) for Au+Au collisions at  $\sqrt{s_{NN}} = 7.7$  - 200 GeV and  $\bar{d}$  (solid markers) for  $\sqrt{s_{NN}} = 27$  - 200 GeV. For  $\sqrt{s_{NN}} = 200$  GeV, circles correspond to 0%-10%, triangles to 10%-40%, and squares to 40%-80% central events. For other collision energies, circles correspond to 0%-30% and squares to 30%-80% central events.

dences are qualitatively similar to those seen in identified hadrons [4, 6], with d and  $\bar{d}$  showing similar behavior for all centralities measured.

### B. Blast wave model

The nuclear fireball model was first introduced by Westfall *et al.* to explain midrapidity proton-inclusive spectra [38]. Later, Siemens and Rasmussen [39] generalized a non-relativistic formula by Bondorf, Garpman, and Zimanyi [40] to explain nucleons and pions as they are produced in a blast wave of an exploding fireball. The blast wave model has evolved since then, with more parameters to describe both  $p_T$  spectra and anisotropic flow of produced particles [41–43]. The blast wave parametrization modeled by the STAR Collaboration [43] has been recently used to fit the  $v_2$  of identified particles [44]. This version of blast wave has four parameters, namely kinetic freeze-out temperature ( $T$ ), transverse expansion rapidity ( $\rho_0$ ), amplitude of its azimuthal variation ( $\rho_a$ ), and the variation in the azimuthal density of the source elements ( $s_2$ ) [44]. The fit parameters obtained from blast wave fits to the  $v_2$  of identified particles are listed in Table 1 of [44]. We have used the same blast wave model and fit parameter values to check whether the blast wave model also reproduces the  $v_2$  of light nuclei measured in the data. Figure 8 shows the blast wave model predictions for light nuclei, along with the measurements. As is evident from Fig. 8, blast wave model under-predicts the  $v_2$  of d and  $\bar{d}$  at low  $p_T$  ( $p_T < 1.0$  GeV/c) for most of the collision energies. Similar conclusion for t,  ${}^3\text{He}$  ( ${}^3\bar{\text{He}}$ ) is difficult to make due to their

large statistical uncertainty. However, for  $\sqrt{s_{NN}} = 200$  GeV, the blast wave model clearly fails to reproduce the measured  $v_2$  of light nuclei of all species at low  $p_T$  ( $p_T < 1.0$  GeV/c).

### C. Atomic mass number scaling and coalescence model

Figure 9 presents the light-nuclei  $v_2/A$  as a function of  $p_T/A$ , where  $A$  is the atomic mass number of the corresponding light nuclei. The main goal of this study is to understand whether light (anti-)nuclei production is consistent with coalescence of (anti-)nucleons. The model predicts that if a composite particle is produced by coalescence of  $n$  number of particles that are very close to each other in phase-space, then  $v_2(p_T)$  of the composite will be  $n$  times that of the constituents [45]. In Fig. 9 it is observed that the (anti-)nuclei  $v_2/A$  closely follows  $v_2$  of p ( $\bar{p}$ ) for  $p_T/A$  up to 1.5 GeV/c. The scaling behavior of these nuclei suggest that d ( $\bar{d}$ ) within  $p_T < 3.0$  GeV/c and t,  ${}^3\text{He}$  ( ${}^3\bar{\text{He}}$ ) within  $p_T < 4.5$  GeV/c might have formed via the coalescence of nucleons (anti-nucleons). The low relative production of light nuclei seems to favor the coalescence formalism rather than other methods, such as thermal production which can reproduce the measured particle ratios in data [46]. As protons and neutrons have the same  $v_2$ , expected from NCQ scaling, then we can readily see that the  $v_2$  of t and  ${}^3\text{He}$  will be the same as they have the same atomic mass number ( $A = 3$ ). We find that, within statistical errors, our measurement of  $v_2(p_T)$  for t and  ${}^3\text{He}$  confirms this assumption. Although simple  $A$  scaling seems to hold for the colli-

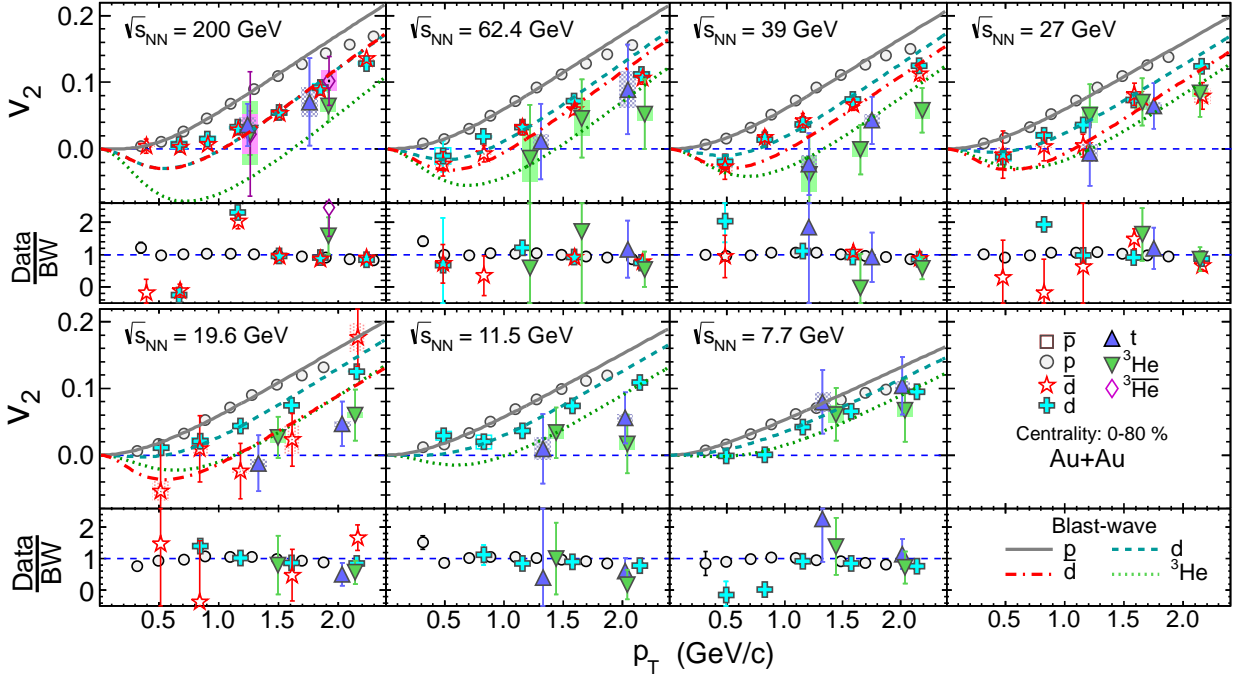


FIG. 8. (color online) Blast wave model predictions (lines) of  $v_2$  for  $d$ ,  $\bar{d}$ ,  $t$ ,  ${}^3\text{He}$  ( ${}^3\bar{\text{He}}$ ) compared with the data for minimum bias Au+Au collisions. The blast wave model and parameter values have been used from [44]. (Some data points in the lower panels are off-scale.)

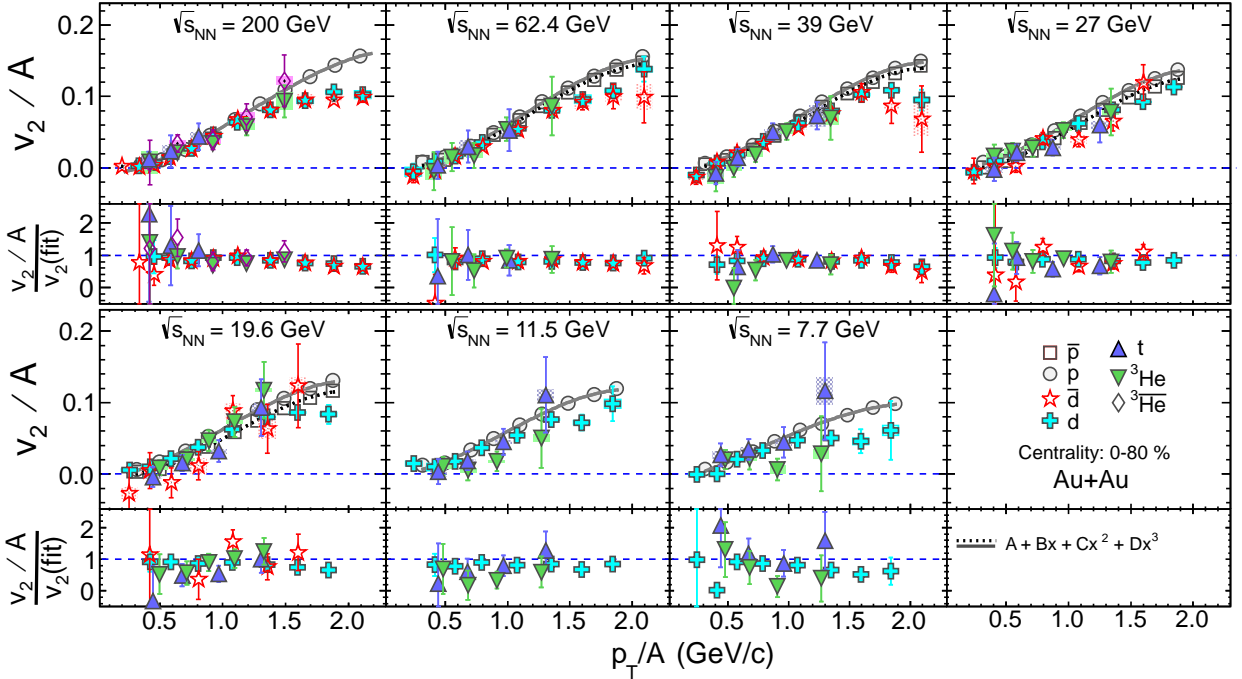


FIG. 9. (color online) Atomic mass number ( $A$ ) scaling of the mid-rapidity  $v_2$  of  $p$ ,  $\bar{p}$ ,  $d$ ,  $\bar{d}$ ,  $t$ ,  ${}^3\text{He}$ , and  ${}^3\bar{\text{He}}$  from minimum bias Au+Au collisions at  $\sqrt{s_{NN}} = 200, 62.4, 39, 27, 19.6, 11.5,$  and  $7.7$  GeV. Grey Solid (black dotted) lines correspond to  $3^{rd}$  order polynomial fits to the  $p$  ( $\bar{p}$ )  $v_2$  data. The ratios of  $[v_2/A]/fit$  for  $d$ ,  $\bar{d}$ ,  $t$ , and  ${}^3\text{He}$  are shown in the lower panels at each corresponding collision energy. (Some data points in the lower panels are off-scale.)

sion energies presented, the actual mechanism might be a more dynamic process including production and coales-

cence of nucleons in the local rest frame of the fluid cell. This scenario might give rise to deviations from simple

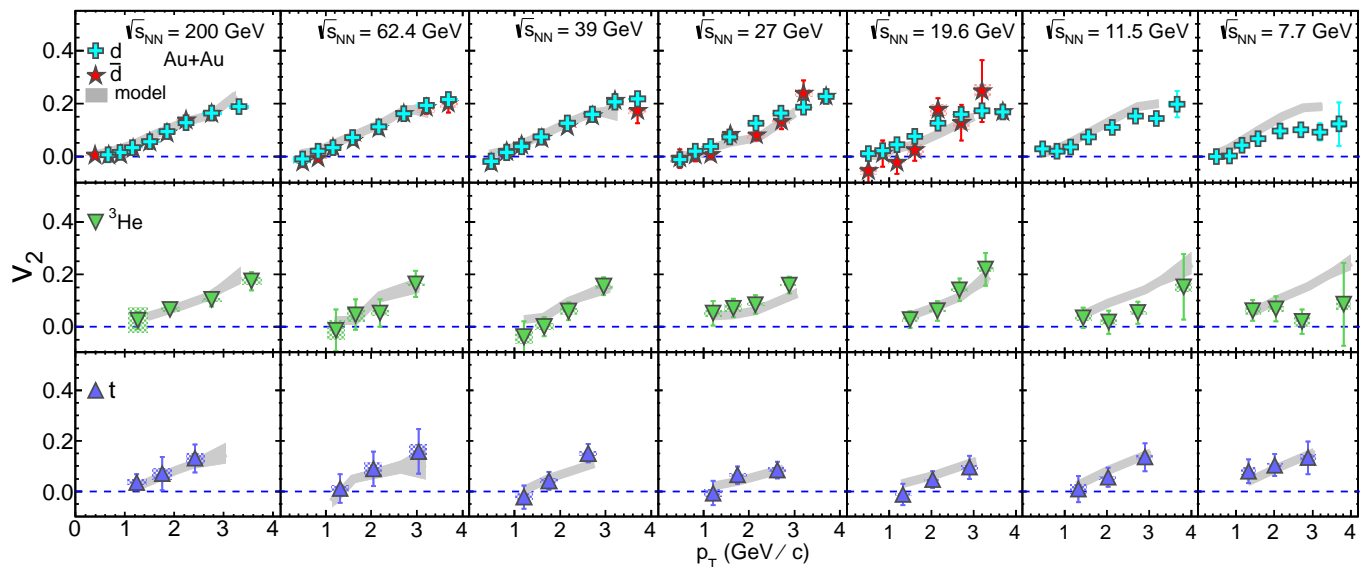


FIG. 10. (color online) Mid-rapidity  $v_2$  of d, t, and  ${}^3\text{He}$  are compared with the results of AMPT+coalescence calculations (solid bands).

A scaling.

It is arguable that light nuclei could have also formed via coalescence of quarks as the scaling behavior holds when  $v_2$  and  $p_T$  are scaled by number of constituent quarks (e.g. 6 for d,  $\bar{d}$  and 9 for t,  ${}^3\text{He}$ ) instead of mass number. Although this process seems physically acceptable, the survival of light nuclei, with their low binding energies ( $\sim$ few MeV), is highly unlikely under the high temperatures requisite for dissociating nucleons into quarks and gluons.

To further verify the applicability of nucleon coalescence into light nuclei in heavy-ion collisions, we have run the string-melting version of A Multi Phase Transport (AMPT, version v1.25t7d) [47] model of the collisions in conjunction with a dynamic coalescence model. The AMPT model has been used to reproduce charged particle multiplicity, transverse momentum spectra at RHIC and LHC, as well as  $v_2$  of identified particles at RHIC [47]. The dynamic coalescence model has been used extensively at both intermediate [48] and high energies [49]. In this model, the probability for producing a cluster is determined by the overlap of the cluster's Wigner phase-space density with the nucleon phase-space distribution at freeze-out procured from AMPT. For light nuclei, the Wigner phase-space densities are obtained from their internal wave functions, which are taken to be those of a spherical harmonic oscillator [50]. For the coalescence model we have used radii of 1.96, 1.61, and 1.74 fm for d, t, and  ${}^3\text{He}$  respectively [51]. These parameters are kept fixed for the collision energy range presented. The model's results for  $v_2$  of d, t, and  ${}^3\text{He}$  are shown as solid bands in Fig. 10. The data and model agree within errors over nearly all energies and  $p_T$  measured, supporting the theory that light nuclei are produced via nucleon coalescence in heavy-ion collisions. Recently the

ALICE collaboration has measured production of d and  $\bar{d}$  in Pb+Pb collisions at  $\sqrt{s_{NN}} = 2.76$  TeV [52]. In that study, light-nuclei spectra were found to exhibit a significant hardening with increasing centrality. The stiffening of light-nuclei spectra at ALICE could be the result of increased hard scattering, modified fragmentation, or increased radial flow. However, the analysis lacks conclusive evidence regarding the production mechanism of light nuclei in heavy-ion collisions. In the collision energy range presented in this paper, light-nuclei production favors the coalescence model.

#### IV. SUMMARY

Measurements of the  $2^{nd}$  order azimuthal anisotropy,  $v_2(p_T)$  at mid-rapidity ( $|y| < 1.0$ ) have been presented for light nuclei d, t,  ${}^3\text{He}$  (for  $\sqrt{s_{NN}} = 200, 62.4, 39, 27, 19.6, 11.5$ , and  $7.7$  GeV), and anti-nuclei  $\bar{d}$  ( $\sqrt{s_{NN}} = 19.6$ – $200$  GeV) and  ${}^3\bar{\text{He}}$  ( $\sqrt{s_{NN}} = 200$  GeV). Similar to hadrons over the measured  $p_T$  range, light (anti-)nuclei  $v_2(p_T)$  show a monotonic rise with increasing  $p_T$ , mass ordering at low  $p_T$ , and a reduction for more central collisions. It is observed that  $v_2$  of nuclei and anti-nuclei are of similar magnitude for  $\sqrt{s_{NN}} = 39$  GeV and above. The difference  $\Delta v_2$  between d and  $\bar{d}$  is found to follow the difference between p and  $\bar{p}$  as a function of collision energy. The blast wave model is found to under-predict the light-nuclei  $v_2$  measured in data.  ${}^3\text{He}$  and t nuclei show similar  $v_2$  for all collision energies, and in fact all the light-nuclei  $v_2$  generally follow an atomic mass number scaling, which indicates that the coalescence of nucleons might be the underlying mechanism of light-nuclei formation in high energy heavy-ion collisions. This observation is further

corroborated by carrying out a model-based study of nuclei  $v_2$  using a transport-plus-coalescence model, which reproduces well the light-nuclei  $v_2$  measured in the data.

### ACKNOWLEDGEMENTS

We thank the RHIC Operations Group and RCF at BNL, the NERSC Center at LBNL, the KISTI Center in Korea, and the Open Science Grid consortium for

providing resources and support. This work was supported in part by the Office of Nuclear Physics within the U.S. DOE Office of Science, the U.S. NSF, the Ministry of Education and Science of the Russian Federation, NSFC, CAS, MoST and MoE of China, the National Research Foundation of Korea, NCKU (Taiwan), GA and MSMT of the Czech Republic, FIAS of Germany, DAE, DST, and UGC of India, the National Science Centre of Poland, National Research Foundation, the Ministry of Science, Education and Sports of the Republic of Croatia, and RosAtom of Russia. This work is supported by the DAE-BRNS project Grant No. 2010/21/15-BRNS/2026.

- 
- [1] M. A. Stephanov, K. Rajagopal, and E. V. Shuryak, Phys. Rev. Lett. **81**, 4816 (1998); M. A. Stephanov, K. Rajagopal, and E. V. Shuryak, Phys. Rev. D **60**, 114028, (1999); M. A. Stephanov, PoS **LAT2006**, 024 (2006), arXiv:hep-lat/0701002; K. Fukushima and T. Hatsuda, Rep. Prog. Phys. **74**, 014001 (2010).
- [2] I. Arsene *et al.* (BRAHMS collaboration), Nucl. Phys. A **757**, 1 (2005); B. B. Back *et al.* (PHOBOS Collaboration), Nucl. Phys. A **757**, 28 (2005); J. Adams *et al.* (STAR Collaboration), Nucl. Phys. A **757**, 102 (2005); K. Adcox *et al.* (PHENIX Collaboration), Nucl. Phys. A **757**, 184 (2005).
- [3] L. Adamczyk *et al.* (STAR Collaboration), Phys. Rev. C **86**, 054908 (2012).
- [4] L. Adamczyk *et al.* (STAR Collaboration), Phys. Rev. C **88**, 014902 (2013).
- [5] L. Adamczyk *et al.* (STAR Collaboration), Phys. Rev. Lett. **110**, 142301 (2013).
- [6] L. Adamczyk *et al.* (STAR Collaboration), arXiv:1509.08397 [nucl-ex].
- [7] A. Adare *et al.* (PHENIX Collaboration), arXiv:1410.2559 [nucl-ex].
- [8] A. Adare *et al.* (PHENIX Collaboration), arXiv:1506.07834 [nucl-ex].
- [9] L. Adamczyk *et al.* (STAR Collaboration), arXiv:1507.05247 [nucl-ex].
- [10] S. A. Voloshin, Nucl. Phys. A **715**, 379 (2003).
- [11] D. Molnar and S.A. Voloshin, Phys. Rev. Lett. **91**, 092301 (2003).
- [12] J. Adams *et al.* (STAR Collaboration), Phys. Rev. Lett. **95**, 122301 (2005).
- [13] X. Dong *et al.*, Phys. Lett. B **597**, 328 (2004); Nu Xu, J. Phys. Conf. Ser. **50**, 243 (2006).
- [14] R. A. Lacey, A. Taranenko, arXiv:nucl-ex/0610029.
- [15] V. Greco, C. M. Ko and P. Lévai, Phys. Rev. C **68**, 034904 (2003).
- [16] H. H. Gutbrod *et al.*, Phys. Rev. Lett. **37**, 667 (1976).
- [17] R. Scheibl and U. Heinz, Phys. Rev. C **59**, 1585 (1999).
- [18] H. Sato and K. Yazaki, Phys. Lett. B **98**, 153 (1981).
- [19] S. T. Butler and C. A. Pearson, Phys. Rev. **129**, 836 (1963).
- [20] W. J. Llope *et al.*, Phys. Rev. C **52**, 2004 (1995).
- [21] S. Afanasiev *et al.* (PHENIX Collaboration), Phys. Rev. Lett. **99**, 052301 (2007).
- [22] B. I. Abelev *et al.* (STAR Collaboration), arXiv:0909.0566v1 [nucl-ex].
- [23] C. Jena (for the STAR collaboration), arXiv:1101.4196 [nucl-ex].
- [24] K. H. Ackermann *et al.* (STAR Collaboration), Nucl. Instrum. Methods A **499**, 624 (2003).
- [25] M. Anderson *et al.* (STAR Collaboration), Nucl. Instrum. Methods A **499**, 659 (2003).
- [26] W. J. Llope, Nucl. Instrum. Methods B **241**, 306 (2005); W. J. Llope, Nucl. Instrum. Methods A **661**, S110 (2012).
- [27] H. Bichsel, Nucl. Instrum. Methods A **562**, 154 (2006).
- [28] W. J. Llope *et al.*, Nucl. Instrum. Methods A **759**, 23 (2014).
- [29] C. Adler *et al.* (STAR Collaboration), Nucl. Instrum. Methods A **470**, 488 (2001).
- [30] C. A. Whitten Jr, AIP Conf. Proc. **980**, 390 (2008); J. Kiryuk, arXiv:hep-ex[0501072].
- [31] D. Kharzeev and M. Nardi, Phys. Lett. B **507**, 121 (2001).
- [32] A. M. Poskanzer and S. A. Voloshin, Phys. Rev. C **58**, 1671 (1998).
- [33] S. A. Voloshin, A. M. Poskanzer and R. Snellings, Collective Phenomena in Non-Central Nuclear Collisions, in Relativistic Heavy Ion Physics, Landolt-Börnstein series, Springer-Verlag, Berlin Germany, Vol. 23, p. 293 (2010), arXiv:0809.2949v2 [nucl-ex].
- [34] P. Danielewicz *et al.*, Phys. Rev. C **38**, 120 (1988); J. Barrette *et al.* (E877 Collaboration), Phys. Rev. C **55**, 1420 (1997); J. Barrette *et al.* (E877 Collaboration), Phys. Rev. C **56**, 3254 (1997).
- [35] B. I. Abelev *et al.* (STAR Collaboration), Phys. Rev. C **81**, 044902 (2010).
- [36] H. Masui and A. Schmah, arXiv:1212.3650v1 [nucl-ex].
- [37] P. F. Kolb and U. Heinz Nucl. Phys. A **715**, 653 (2003).
- [38] G. D. Westfall *et al.*, Phys. Rev. Lett. **37**, 1202 (1976).
- [39] P. J. Siemens and J. O. Rasmussen, Phys. Rev. Lett. **42**, 880 (1979).
- [40] J. P. Bondorf, S. I. A. Garpman, and J. Zimanyi, Nucl. Phys. A **296**, 320 (1978).
- [41] E. Schnedermann, J. Sollfrank, and U. Heinz, Phys. Rev. C **48**, 2462 (1993).
- [42] P. Huovinen, P. F. Kolb, U. Heinz, P. V. Ruuskanen, and S. Voloshin, Phys. Lett. B **503**, 58 (2001).
- [43] C. Adler *et al.* (STAR Collaboration), Phys. Rev. Lett. **87**, 182301 (2001).
- [44] X. Sun, H. Masui, A. M. Poskanzer, and A. Schmah, Phys. Rev. C **91**, 024903 (2015).

- [45] T. Z. Tan *et al.*, Phys. Lett. B **638**, 50 (2006).
- [46] S. Chatterjee and B. Mohanty, Phys. Rev. C **90**, 034908 (2014).
- [47] Z. Lin, C. M. Ko, B. A. Li, B. Zhang, and S. Pal, Phys. Rev. C **72**, 064901 (2005).
- [48] M. Gyulassy, K. Frankel, E. A. Remler, Nucl. Phys. A **402**, 596 (1983); J. Aichelin *et al.*, Phys. Rev. Lett. **58**, 1926 (1987); V. Koch *et al.*, Phys. Lett. B **241**, 174 (1990); L. W. Chen, C.M. Ko, B. A. Li, Phys. Rev. C **68**, 017601 (2003).
- [49] J. L. Nagle *et al.*, Phys. Rev. C **53**, 367 (1996); R. Mantiello, H. Sorge, H. Stöcker, and W. Greiner, Phys. Rev. C **55**, 1443 (1997); L. W. Chen and C. M. Ko, Phys. Rev. C **73**, 044903 (2006).
- [50] R. Scheibl and U. Heinz, Phys. Rev. C **59**, 1585 (1999); A. T. M. Aerts and C. B. Dover, Phys. Rev. D **28**, 450 (1983).
- [51] Lie-Wen Chen, C. M. Ko and Bao-Ali n Li, Nucl. Phys. A **729**, 809 (2003).
- [52] J. Adam *et al.* (ALICE Collaboration), arXiv:1506.08951 [nucl-ex].